

## Evidence for massive warm-hot circumgalactic medium around NGC 3221

SANSKRITI DAS,<sup>1</sup> SMITA MATHUR,<sup>1,2</sup> ANJALI GUPTA,<sup>1,3</sup> FABRIZIO NICASTRO,<sup>4,5</sup> YAIR KRONGOLD,<sup>6</sup> AND CODY NULL<sup>3</sup>

<sup>1</sup>*Department of Astronomy, The Ohio State University, 140 West 18th Avenue, Columbus, OH 43210, USA*

<sup>2</sup>*Center for Cosmology and Astroparticle Physics, 191 West Woodruff Avenue, Columbus, OH 43210, USA*

<sup>3</sup>*Columbus State Community College, 550 E Spring St., Columbus, OH 43210, USA*

<sup>4</sup>*Observatorio Astronomico di Roma - INAF, Via di Frascati 33, 1-00040 Monte Porzio Catone, RM, Italy*

<sup>5</sup>*Harvard-Smithsonian Center for Astrophysics, 60 Garden St., MS-04, Cambridge, MA 02138, USA*

<sup>6</sup>*Instituto de Astronomia, Universidad Nacional Autonoma de Mexico, 04510 Mexico City, Mexico*

### ABSTRACT

We report a  $3.4\sigma$  detection of the warm-hot, massive, extended circumgalactic medium (CGM) around an L<sup>\*</sup> star-forming spiral galaxy NGC 3221, using deep *Suzaku* observations. The temperature of the gas is  $10^{6.1}$  K, comparable to that of the Milky Way CGM. The spatial extent of the gas is at least 150 kpc. For a  $\beta$ -model of density profile with solar abundance, the central emission measure is  $EM = 3 \pm 1 \times 10^{-5} \text{ cm}^{-6} \text{ kpc}$  and the central electron density is  $n_{eo} = 4 \pm 1 \times 10^{-4} \text{ cm}^{-3}$ , with a slope of  $\beta = 0.56$ . We investigate a range of  $\beta$  values, and find that the details of the density profile do not change our results significantly. The mass of the warm-hot gas, assuming a metallicity of  $\frac{1}{3} Z_{\odot}$  is  $16 \pm 3 \times 10^{10} M_{\odot}$ , being the most massive baryon component of NGC 3221. The baryon fraction is  $f_b = 0.120 \pm 0.036$  (statistical)  $^{+0.104}_{-0.048}$  (systematic), consistent with the cosmological mean value, closing the baryon budget of this galaxy. We also investigated the missing metals problem in conjunction with the missing baryons problem and conclude that metals are likely to be preferentially expelled from the galaxy. Ours is the first detection of an extended warm-hot CGM around an external L<sup>\*</sup> star-forming spiral galaxy, where the CGM likely accounts for the missing galactic baryons.

*Keywords:* missing baryons — diffuse emission — soft X-rays: CGM — individual: NGC 3221 — star-forming galaxy — L<sup>\*</sup> galaxy

### 1. INTRODUCTION

It has been known from observations that the nearby galaxies are missing most of their baryons. The stellar and ISM (interstellar medium) components account for a small fraction of the total baryons (Tumlinson et al. 2017), compared to the amount expected from the universal baryon fraction of  $\Omega_b/\Omega_m = 0.157 \pm 0.001$  (Planck Collaboration et al. 2016). The missing metals problem comes alongside the missing baryons problem; nearby galaxies are short of metals as expected from the star formation history of the universe (Shapley et al. 2003). It is also related to the problem of missing feedback (Wang 2010), where the fate of the star-formation driven outflow remains untraced. A possible solution to all of these problems lies in the highly ionized warm-hot circumgalactic medium (CGM) extended out to the virial

radius of the galaxies, as has been predicted by theoretical models (White & Rees 1978; Ford et al. 2014; Oppenheimer et al. 2016; Suresh et al. 2017). The CGM of galaxies is supposed to be a large reservoir of warm-hot gas, and can account for  $\approx 40\%$  of metals produced by star-forming galaxies (Peeples et al. 2014). This warm-hot ( $T = 10^6$ - $10^7$  K) phase can be probed by highly ionized metals (e.g. O VII and O VIII), the dominant transitions of which lying in the soft X-ray band. Deep X-ray observations in emission and absorption are necessary to distinguish between different sources of the missing baryonic mass and characterize the medium as a function of the host galaxy properties with a broad parameter space. The distribution of the density, metallicity and temperature, the spacial extent, and the mass of this warm-hot gas provide important constraints to the models of galaxy formation and the accretion and feedback mechanisms.

The search for missing mass in the form of warm-hot gas beyond the optical radii of galaxies started with

**Table 1.** Basic properties of NGC3221 (Taken from [Lehmer et al. 2010](#))

Type	Location ( $l, b$ )	$D_L$ (Mpc)	Size	$\log M_*$ ( $M_\odot$ )	SFR ( $M_\odot \text{yr}^{-1}$ )
SBcd	(213.97°, 55.71°)	59.46	3.2'×0.7'	11.00±0.10	9.92±1.00

*ROSAT* and continued with *Chandra*, *XMM-Newton* and *Suzaku*. However, unlike the rich galaxy clusters ([White et al. 1993](#)) and the massive early-type galaxies ([Forman et al. 1985](#); [Humphrey et al. 2012](#)), where ample amount of hot gas dominates the baryonic component of the system and retains the cosmological allotment of baryons, the X-ray coronae around spirals are faint, which makes their detection challenging. While the warm-hot CGM detected around the Milky Way may account for the missing mass ([Gupta et al. 2012, 2014](#); [Nicastro et al. 2016b](#); [Gupta et al. 2017](#)), the extended CGM in X-ray emission has been confidently detected only around massive galaxies ( $M_* > 2 \times 10^{11} M_\odot$ ), and only out to a fraction of their virial radii, with mass insufficient to close their baryonic budget ([Anderson & Bregman 2011](#); [Dai et al. 2012](#); [Bogdán et al. 2013b,a](#); [Anderson et al. 2016](#); [Bogdán et al. 2017](#); [Li et al. 2017a, 2018](#)).

In this paper, we search for hot diffuse gas around an L\* spiral galaxy NGC 3221. The basic properties of the galaxy are given in Table 1. It is an actively star-forming galaxy with a high star-formation rate. It has a high ratio of  $L_{FIR}/D_{25}^2 = 13.8 \times 10^{40} \text{ erg s}^{-1} \text{ kpc}^{-2}$  where  $L_{FIR}$  is the far-infrared luminosity and  $D_{25}$  is the diameter out to the surface brightness of 25 mag arcsec $^{-2}$ . Additionally, it has a high ratio of flux densities at 60 and 100 microns,  $S_{60}/S_{100} = 0.37$ , confirming that NGC 3221 is an actively star-forming galaxy ([Rossa & Dettmar 2003](#)).

Our paper is structured as follows: we discuss the data reduction and analysis in section 2 and 3, starting with data reduction followed by the point source identification, imaging analysis and spectral analysis of the diffuse medium from the *Suzaku* data. Then we report the detection of the CGM emission, model its radial profile and derive some of its physical properties in section 4. Our findings are interpreted in the context of missing baryons, missing metals and missing feedback problems in section 5. Then, we compare our result with earlier observations in section 6. We summarize our results and outline some of the future aims in the last section.

## 2. OBSERVATIONS AND DATA REDUCTION

### 2.1. *Suzaku* Observations

We observed the field of NGC 3221 with *Suzaku*. As noted above, the emission signal from the CGM is expected to be faint, dominated by foreground/background.

To characterize the foreground and background, we also observed two fields  $\approx 2$  deg away from the galaxy. From now on, we will refer to the field of the galaxy as the galaxy-field and the other two fields as off-fields. With the deep *Suzaku* observations, our goal is to extract the emission signal from the CGM of NGC 3221, and the off-fields are used to determine the foreground/background emission. We expect to detect emission from about a million degree thermal plasma, with the most dominant signature being the emission lines of O VII and/or O VIII around 0.5–0.6 keV. Therefore, the soft X-ray band is important for our analysis, as discussed below.

The large field of view (FOV  $\approx 17.8' \times 17.8'$ ), low and stable detector background, and high sensitivity to detect low surface brightness in soft X-rays have made *Suzaku* an excellent choice to study the diffuse circumgalactic medium. The back-illuminated X-ray Imaging Spectrometer (XIS-1) with largest effective area among all other chips at our energy range of interest (0.4–5.0 keV) serves the best for this purpose. We observed the NGC 3221 galaxy-field and off-field2 in November, 2014 and off-field1 in May, 2014. The unfiltered exposure time of the galaxy-field and the off-fields are  $\approx 121$  ks, 41 ks and 40 ks respectively.

### 2.2. Data Reduction

We reduced the data very carefully taking into account the changes in XIS-1 instrumentation with time and also the effect of enhanced solar activity on the post-2011 observations of a low earth-orbit ( $\approx 550$  km) satellite like *Suzaku* (Appendix A).

Our first task was to identify and remove the point sources in the three observed fields. We identify the compact bright sources in 0.4–0.7 keV, 0.7–1.0 keV and 1.0–2.0 keV bands separately. We smoothed the images with Gaussian kernel radius of 5 to identify sources  $\geq 3\sigma$  brighter than their background (figure 1). We smoothed all sources upto the spatial resolution of *Suzaku* (PSF  $\approx 1.8'–2.0'$ , half power diameter, or radius of  $0.9'–1.0'$ ) unless the source itself appeared larger, and removed the contribution of all sources from the respective fields. Point source contamination in the hard ( $>2$  keV) band is modeled spectroscopically, as discussed below in §3.1. The projected semi-major axis of the stellar disk of NGC 3221 is  $1.6' \approx 25$  kpc. To separate the large scale diffuse X-ray emission of the CGM from the emission of the stellar disk and the extra-planar region between

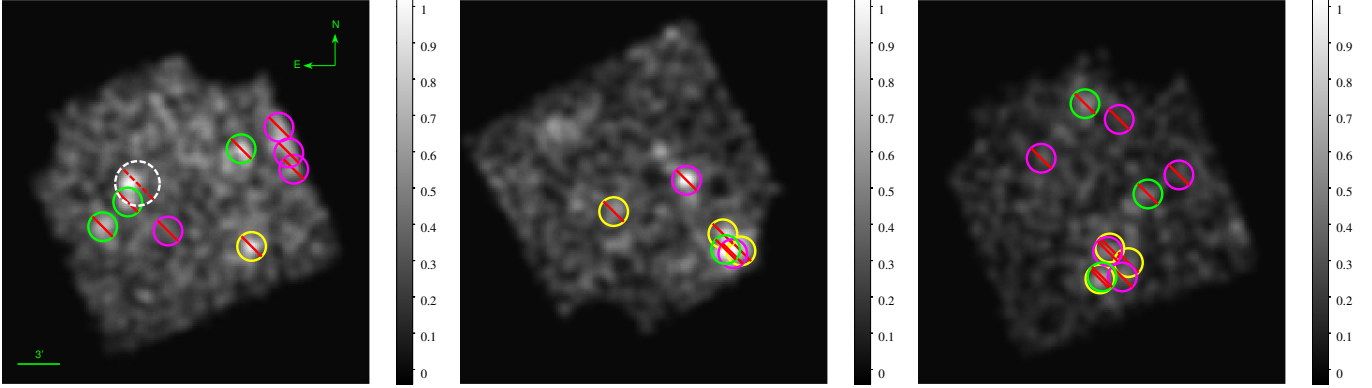


**Figure 1.** 0.4-2.0 keV images of the *Suzaku* fields (left: galaxy-field, middle & right: off-fields). Point sources identified in 0.4-0.7 keV, 0.7-1.0 keV and 1.0-2.0 keV are shown in magenta, yellow and green respectively, smoothed to the PSF. The white dashed circle in the galaxy-field covers the optical extent of NGC 3221. The sky direction and the angular scale ( $16 \text{ kpc} \approx 1'$ ) are shown in the left panel

5.5 kpc (the semi-minor axis of NGC 3221) and 25 kpc, we remove a circular region of 25 kpc radius around the center of NGC 3221 in the galaxy-field. The excluded region is significantly larger than the *Suzaku* PSF, therefore we do not expect the emission from the stellar disk of NGC 3221 to contaminate the emission from the extended CGM beyond the radii of  $1.6'$ . We construct the count-rate histogram of events observed in 0.4-2.0 and 2.0-5.0 keV bands. We find that there are  $\approx 3\%$  events outside  $2\sigma$  limit of mean count rate in all the three fields in both the energy ranges, well within the distribution of Poisson fluctuations.

### 3. ANALYSIS

We have done the data analysis in two steps: imaging and spectral analysis. Before we delve into spectral analysis to extract the CGM signal, we study the radial and angular profile of the soft X-ray imaging data. We clarify that this data is not foreground/background-subtracted. However, as the foreground/background is not spatially correlated with the target galaxy, they are unlikely to show any radial/azimuthal variation with respect to the position of NGC 3221.

#### 3.1. Imaging Analysis

The largest complete annular region we can extract is between 25 kpc and 100 kpc. To study the azimuthal variation of emission, we split this annular region into 8 wedges each with an opening angle of  $45^\circ$  (figure 2). The surface brightness in 0.4-1.0 keV is shown in figure 3, with a data point for each wedge. The red line shows the average surface brightness ( $3.80 \pm 0.15 \times 10^{-8} \text{ counts cm}^{-2} \text{ s}^{-1} \text{ arcsec}^{-2}$ ), with the shaded region showing  $1\sigma$  error. The surface brightness in sectors 1, 2, 3, 5 and 6 agrees with each other within statistical uncertainties, indicating that the extended emission is fairly

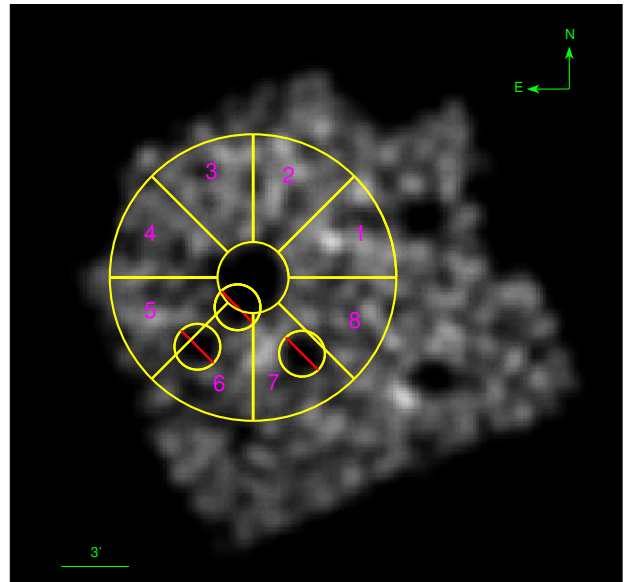


**Figure 2.** Wedges to study the azimuthal surface brightness profile. The inner and outer radial boundaries of the wedges correspond to 25 kpc and 100 kpc from the galaxy. The sky direction and angular scale are shown in the top-right and bottom-left corners respectively

uniform. There is an apparent increase of the surface brightness in sector 7; we interpret this as due to the contamination from a soft compact source leaked beyond the half-power diameter of  $2'$  (see figure 1, top panel). The sectors 4 and 8 have a mean surface brightness =  $3.05 \pm 0.25 \times 10^{-8} \text{ counts cm}^{-2} \text{ s}^{-1} \text{ arcsec}^{-2}$ , shown by the dash-dotted line, with the purple shaded region showing  $1\sigma$  uncertainty. This is  $\approx 40\%$  smaller than the global average, but is only  $2\sigma$  from the mean, so we do not draw any strong inference from this deviation. We note, however, that these sectors are along the minor axis of NGC 3221, so the low surface bright-

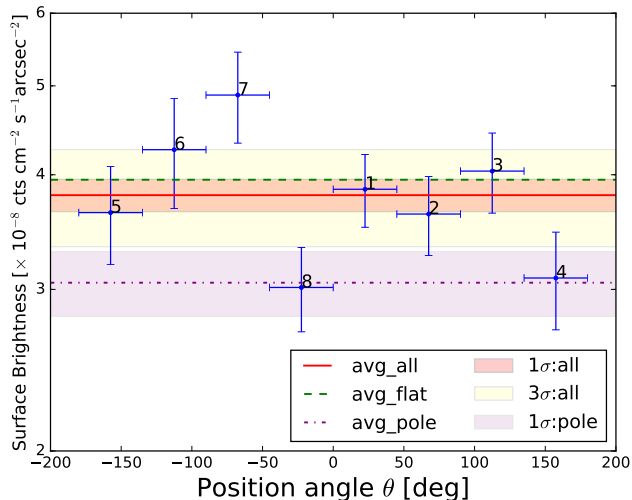


**Figure 3.** Azimuthal surface brightness profile in 0.4-1.0 keV, with the wedges labeled as in figure 2. The global mean (avg-all) is shown with the red horizontal line and  $1\sigma$  and  $3\sigma$  regions are shown with orange and yellow regions, respectively. Sectors 4 and 8 are along the minor axis of the galaxy, with significantly lower surface brightness; their average (avg\_pole; dash-dotted line) and the  $1\sigma$  region are shown in purple. Sector 7 and 8 are  $3\sigma$  away from the global average. The average of sectors 7 and 8 (avg\_flat) is shown with the dashed green line. As discussed in the text, these azimuthal variations do not affect the determination of the radial profile.

ness could be the manifestation of a cavity created by the bipolar outflow from this star-forming galaxy. Such a cavity has been observed in the Milky Way (Nicastrò et al. 2016a). Overall, the uniform distribution is morphologically consistent with the quasi-static warm/hot gas residing in the potential well of the galaxy.

To study the radial variation of the surface brightness in 0.4–1.0 keV, we extract 9 annular regions of similar geometric area (i.e.  $(r_{out}^2 - r_{in}^2)$  is constant) between 25 kpc and 160 kpc. The azimuthal variations discussed above are averaged out. The surface brightness remains almost flat near the core and then slowly decreases with distance from the galaxy (figure 4). Although the surface brightness is dominated by the foreground/background, its contamination over the FOV in the galaxy-field should be constant. The transverse radial variation of the surface brightness with respect to the galaxy’s position indicates the existence of a medium related to NGC 3221. Otherwise, a flat radial surface brightness profile would indicate that the halo emission from NGC 3221 is too faint to be detected, which is not the case. Therefore, we fit the surface brightness profile for two density distributions, with a truncated constant density medium and with a  $\beta$ -model. For the homoge-

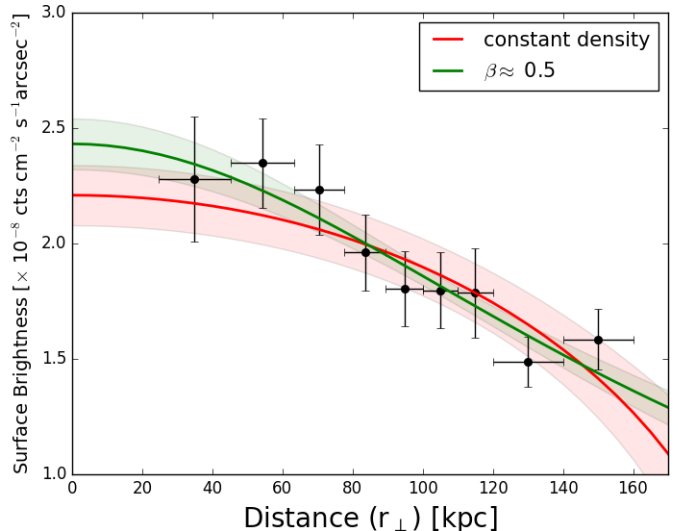


**Figure 4.** Radial surface brightness profile of NGC 3221 in 0.4-1.0 keV. The shaded regions represent 68% confidence interval, considering the uncertainties in the best-fitted values of each model’s free parameters

neous (constant density) medium, we use equation 1:

$$S(r) = S_o \sqrt{1 - (r_{\perp}/R_{out})^2} \quad (1)$$

where  $R_{out}$  is the spatial extent of the gaseous medium. For the  $\beta$ -model we use equation 2 (Sarazin 1986):

$$S(r) = S_o (1 + (r_{\perp}/r_c)^2)^{-3\beta+0.5} \quad (2)$$

where  $S_o$  is the central surface brightness,  $r_c$  is the core radius and  $r_{\perp}$  is the projected distance across the line of sight. The best-fit values ( $\chi^2/dof = 7.07/7$ ) for the constant density model are :  $S_o = (2.2 \pm 0.1) \times 10^{-8}$  counts  $\text{cm}^{-2} \text{s}^{-1} \text{arcsec}^{-2}$  and  $R_{out} = 195 \pm 14$  kpc. We fit the  $\beta$ -model as follows. We first fix  $\beta = 0.5$  as is usually done in literature (see Gupta et al. (2017) and references therein) and fit the radial profile for  $S_o$  and  $r_c$ . The best-fit value of  $r_c$  is  $178 \pm 17$  kpc. Then we fix  $r_c$  at 178 kpc and fit for  $S_o$  and  $\beta$ . The resulting best-fit values ( $\chi^2/dof = 3.76/7$ ) of the parameters are:  $S_o = (2.4 \pm 0.1) \times 10^{-8}$  counts  $\text{cm}^{-2} \text{s}^{-1} \text{arcsec}^{-2}$ , and  $\beta = 0.50 \pm 0.05$ . The central surface brightness is the aggregated emission from the foreground, background and the halo emission, while the radial parameters ( $R_{out}$ ,  $r_c$  and  $\beta$ ) are the characteristics of the density profile of the NGC 3221 halo. This is further confirmed with the spectral analysis below.

### 3.2. Spectral Analysis

For the spectral analysis we generate the non-X-ray background (NXB) and the redistribution matrix function (RMF) for each field (see the details in appendix

A). We then rebin each spectrum such that there is no bin with zero variance, and any spectral information is not lost due to over-smoothing. As the effective area of XIS is very small below 0.4 keV and the detector background is quite high above 5.0 keV, we concentrate on the energy range of 0.4-5.0 keV, for spectral analysis.

The spectra of the diffuse background are complicated, including multiple components which are spectroscopically resolved (Henley et al. 2010; Henley & Shelton 2013; Gupta et al. 2014; Henley et al. 2015; Henley & Shelton 2015; Gupta et al. 2017). Our goal is to detect the CGM around NGC 3221, but the galaxy-field spectrum contains the CGM emission plus all the background and foreground emission present in the off-fields. Therefore, we first fit the off-fields spectra and then use those models in fitting the galaxy-field spectrum. Accordingly, we fit the off-field spectra as a composite of three components:

- 1) The foreground consists of the local hot bubble (LHB) and solar wind charge exchange (SWCX). As the target is at a relatively low ecliptic latitude ( $\beta = 10.62^\circ$ ), the heliospheric SWCX is likely present in soft X-ray. But, it does not appear to contribute significantly to the Oxygen lines of interest (Miller & Bregman 2015). The components of LHB and SWCX cannot be separated at the spectral resolution (FWHM  $\approx 0.05$  keV at 1 keV) of XIS (Yoshino et al. 2009). So, the combined emission from the LHB and SWCX is modeled as an unabsorbed collisionally-ionized plasma in thermal equilibrium. We fix the temperature of this component at  $k_B T = 0.099$  keV and the metallicity at solar (see Gupta et al. 2014; Henley & Shelton 2015; Gupta et al. 2017).
- 2) Collisionally ionized plasma in thermal equilibrium, representing the warm-hot gaseous halo of the Milky Way (MWH), absorbed by the Galactic ISM. Again, we fix the metallicity at solar. The normalization factor of the thermal plasma model is metallicity-weighted, so the exact value of the input metallicity does not matter. Our aim is to merely include the contribution of the MWH in the spectral analysis and keeping  $Z = Z_\odot$  does not affect the final result.
- 3) Absorbed power law to account for the unresolved extragalactic point sources, forming the cosmic X-ray background (CXB). We keep the normalization and the power law index as a free parameter.

We model the thermal plasma using Astrophysical Plasma Emission Code (`apec`), which predicts the emission spectrum of optically thin diffuse gas in collisional ionization equilibrium using the atomic data from the

Astrophysical Plasma Emission Database (APED)<sup>1</sup>. We obtain the Galactic column density values,  $N(\text{H I})$ , toward our fields from the general tools of HEASARC. We also take into account thermal line broadening while fitting the spectra.

In the top panel of figure 5, we show the off-field2 spectrum with the best fitted model containing the three components noted above. A significant excess in the data around 0.5 keV is clearly seen, leading to a very poor fit ( $\chi^2/dof = 195.91/105$ ) and poorly constrained parameter values. This could not be adjusted either by varying the temperature of the LHB+SWCX, or by fixing the temperature of the MWH or allowing the metallicity to vary; this shows that the excess is not related to either of the plasma models. We identify the excess as the contamination by O I fluorescent line at 0.525 keV which is created by fluorescence of solar X-rays with neutral Oxygen in the Earth's atmosphere, discussed further below.

Sekiya et al. (2014) pointed out that due to the increased solar activity the flux of O I line at  $\approx 0.525$  keV has increased with time since 2011 in the *Suzaku*/XIS observations. Since XIS cannot distinguish the O I line from the O VII  $K\alpha$  triplet line (forbidden, intercombination and resonance lines at 0.561, 0.569 and 0.574 keV respectively) owing to its energy resolution of  $\approx 0.05$  keV, unless the O I fluorescent line is taken into account, the O VII line intensity would be significantly overestimated. As shown in the top panel of figure 5, we confirm the findings of Sekiya et al. (2014), now with a more robust spectral modeling (including LHB+SWCX, MWH and CXB components) and in a larger wavelength window. This reinforces the importance of considering O I line contamination in the post-2011 data.

From here onward, we include in the spectral model an unabsorbed Gaussian emission line fixed at 0.525 keV for the O I fluorescent line. So, the off-fields now have 4 spectral components: O I line, LHB+SWCX, MWH and CXB. We fit the off-field spectra again and obtain a good fit ( $\chi^2/dof = 102.68/105$ ), as shown in the bottom panel of figure 5. The best fit model of the off-field defines the background plus foreground model for the galaxy field.

Next, we simultaneously fit the galaxy-field between 25 kpc and 200 kpc of NGC 3221, and the off-fields spec-

<sup>1</sup> The atomic database (<http://www.atomdb.org/physics.php>) includes APED and the spectral models output from the `apec`. The APED files contain information such as wavelengths, radiative transition rates, and electron collisional excitation rate coefficients. `apec` uses these data to calculate spectra. `apec` outputs separate continuum and line emissivity files, making it easy to model continuum and line emission separately as well as together

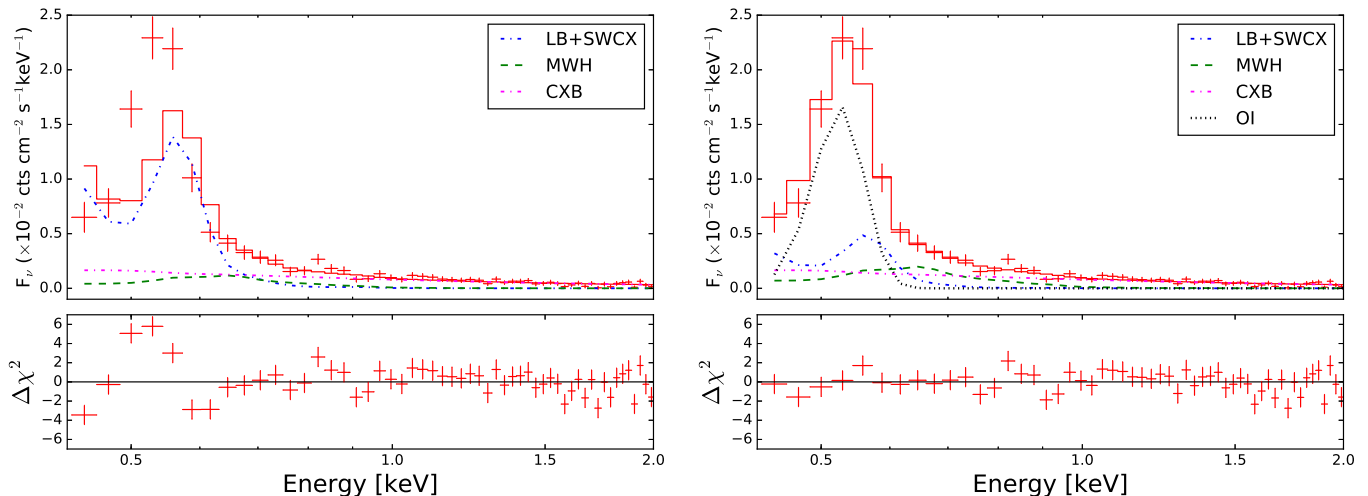


**Figure 5.** Soft spectrum of off-field 2 (covering the whole FOV) and the best-fitted models without (left) and with (right) the O I line. In the absence of O I line the contribution of LHB+SWCX is overestimated (top) to adjust the excess due to O I

tra. We use the best-fit models of the off-fields as initial guesses. While the off-fields have 4 spectral components, the galaxy-field has 5 spectral components. In the galaxy-field, we add an `apec` component at the same redshift of NGC 3221, absorbed by the Galactic ISM, representing the CGM of NGC 3221. The free parameters are the temperature and metallicity-weighted normalization factor. The O I line intensity depends on the solar activity during the observations, so we do not tie it in the galaxy-field and the off-fields. As the fields are separated by only 2deg, we do not expect any significant change in the LHB+SWCX component between the off-fields and the galaxy-field. So, we constrain this component to be the same in the galaxy-field and the off-fields. It is known from previous measurements (Yoshino et al. 2009; Henley & Shelton 2013; Gupta et al. 2014; Henley & Shelton 2015; Gupta et al. 2017) that the temperature of the MWH remains almost constant while the emission measure can vary by more than an order of magnitude along different sightlines. Therefore, we force the temperature of MWH in the off-fields and the galaxy-field to be the same and let the normalization factor vary within the observed range (Henley & Shelton 2013, 2015). The CXB is allowed to be different in the galaxy-field and the off-fields. Tying it to be same did not produce any appreciable change in the fit.

## 4. RESULTS

### 4.1. Detection of the signal

With the spectroscopic modeling discussed above, we isolate the signal from the CGM of NGC 3221. Against the background/foreground defined by off-field1, the emission integral of the galaxy CGM is found to be  $1.1_{-0.3}^{+0.4} \text{ cm}^{-6} \text{ kpc}^3$ , a  $3.4\sigma$  detection (note that the ob-

**Table 2.** Best-fit values <sup>a</sup> of the CGM component

Reference	kT [keV]	EI [ $\text{cm}^{-6} \text{kpc}^3$ ] <sup>b</sup>	$\chi^2/\text{dof}$
off1	$0.115_{-0.014}^{+0.023}$	$1.105_{-0.323}^{+0.359}$	179.78/195
off2	$0.121_{-0.022}^{+0.034}$	$0.617_{-0.359}^{+0.313}$	206.30/194

<sup>a</sup>Obtained for the whole field, extended out to  $\approx 200$  kpc around the disk of NGC 3221

<sup>b</sup>Emission Integral (EI= $\int n^2 dV$ ) is calculated from the best-fitted value of the normalization factor of the APEC component of spectra CGM, using the equation:  $norm = \frac{10^{-14}}{4\pi D^2} \times EI$ , where D is the comoving distance to NGC 3221

served emission integral is degenerate with metallicity; the numbers quoted here are for solar metallicity). Against off-field2, we detect the CGM signal at  $\approx 2\sigma$  significance, with  $EI = 0.6_{-0.4}^{+0.3} \text{ cm}^{-6} \text{ kpc}^3$ . On average, the halo emission integral in the whole field is  $\approx 0.86 \pm 0.24 \text{ cm}^{-6} \text{ kpc}^3$ , showing a significance of  $3.6\sigma$ . The measured temperature against off-field1 and off-field2 are consistent with each other:  $\log(T/K) = 6.1_{-0.2}^{+0.3}$  against off-field1 and  $6.1_{-0.2}^{+0.4}$  against off-field2 (90% confidence interval). We find that while the O I contamination in the off-field1 and the galaxy-field are similar within a factor of  $\approx 1.5$ , it is larger by a factor of  $\approx 3$  in the off-field2 (figure 6). As the position and characteristics of the active regions of the solar corona differ by day, it is conceivable that the flux of solar X-ray and the resulting O I fluorescent line are different in these fields, which are not observed at the same time. Therefore, in further discussions, we use the results of the fit using only the off-field1 as the reference; it gives us better constrained and consistent parameter values.

The above analysis shows that we can determine the EI of the CGM of NGC 3221 with  $3.4\sigma$  significance, once detected. However, it does not tell us whether the sig-

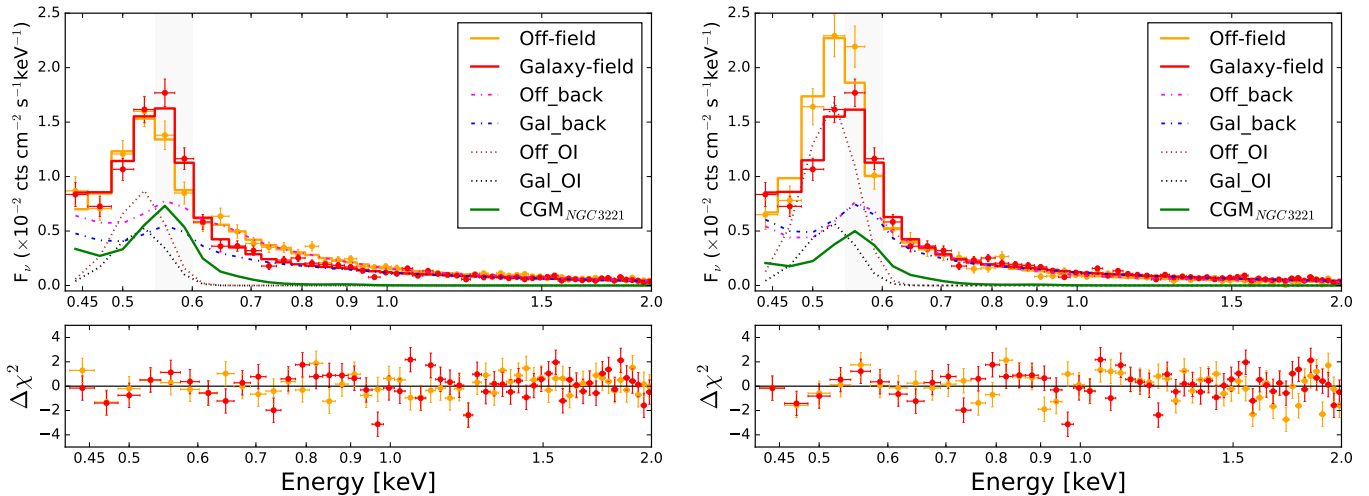


**Figure 6.** Background subtracted spectra of the whole *Suzaku* fields, galaxy-field extending out to  $\approx 200$  kpc from the center of NGC 3221, (left: galaxy-field and the off-field 1, right: galaxy-field and the off-field 2) with the best-fitted models. The combined emission from the foreground and the background (LHB+SWCX+CXB) has been denoted as *back* in the legend. An excess around 0.575 keV in the galaxy-field with respect to the off-field is prominent in the left panel, indicating the existence of the CGM signal. Because of larger O I contamination in the off-field2, the wing of the O I line centered at 0.525 keV overlaps with the O VII line at 0.575 keV (right panel), making the presence of the CGM signal not visually evident in the spectrum

nal from the galaxy’s CGM is required in the spectral model. To assess the same, we performed an F-test with models excluding/including the CGM component. We obtained an F statistic value = 15.3525, for 196 dof, with a null-hypothesis probability of 0.00012 when fitted against the off-field1. This confirms the detection of the CGM of NGC 3221 with 99.988% confidence (this is statistical significance only; as discussed above, there are also systematic uncertainties in determining the foreground/background).

#### 4.2. Confirmation as the extragalactic signal

While the detection of a signal in the galaxy-field is confirmed, the poor spectral resolution of XIS makes it difficult to distinguish between a local and an extragalactic emission. Therefore, to further confirm that the detection is truly from the CGM of NGC 3221, we consider the following possibilities.

- 1) The emission cannot be from the 0.525 keV O I line, as that is already included in the spectral model, and is contributing to the 0.575 keV emission folded through the instrumental profiles. Also, the O I emission peaking at  $\approx 0.575$  keV would imply a huge blueshift ( $v \sim 0.1c$ ), which is extremely unlikely.
- 2) The geocoronal SWCX has a characteristic O VII emission at 0.575 keV. However, the geocoronal emission depends on the solar wind proton flux (Henley & Shelton 2015). As the average proton flux during the galaxy-field observation is lower than the proton fluxes during the off-field observations (figure 9), the geocoronal SWCX

is expected to be lower in the galaxy-field than the off-fields. So, the excess emission in the galaxy-field is unlikely to be associated with geocoronal SWCX. Rather, assuming similar foreground in the galaxy-field and the off-fields makes our detection conservative.

3) The temperature of the detected signal in the galaxy-field is comparable with that of the LHB. Therefore, the signal may be attributed to the variation of the LHB emission. However, as the observed fields are separated by  $\sim 2$  deg, this would imply a density and/or path length fluctuation of LHB at a length scale of 3–7 pc. Such small scale inhomogeneity and anisotropy of the LHB has not been observed (Kuntz & Snowden 2000; Snowden et al. 2014; Liu et al. 2017). So, the detected emission is possibly not from the LHB, although we cannot rule it out completely.

4) The temperature of the detected signal in the galaxy-field ( $10^{6.1}$  K) is consistent with the temperature of the MWH measured from *ROSAT* maps (Snowden et al. 2000; Kuntz & Snowden 2000), and is well within the temperature distribution of the MWH (Henley & Shelton 2013). Therefore, we cannot rule out the possibility that the detected signal is from the halo of Milky Way, and not from NGC 3221. However, the temperature of the MWH in our off-fields and the galaxy-field ( $10^{6.3-6.4}$  K) are higher than the temperature of the detected signal. Therefore, if the detected signal is from the MW CGM, it would imply that the galaxy-field has two distinct temperature components of the MWH, while the

2 nearby off-fields have only temperature component of the MWH; which is highly unlikely.

From the above discussion we can conclude, both physically and statistically, that the detected signal is highly likely to be extragalactic, from the CGM of NGC 3221.

Excited by the first ever detection of the CGM around NGC 3221, we now determine the radial profile of the EI. For this purpose, we select several annular regions of 25 kpc inner radius (transverse distance  $r_{\perp}$ ) and 50, 75, 100, 125, 150, and 200 kpc outer radius in the galaxy-field. In the off-fields, we select the corresponding regions of similar geometric area and perform similar spectral analysis as discussed above (§3.2) for the whole field. For each annular region in the galaxy field, we use a corresponding annular region in the off-field to model the background/foreground. We allow each component of the spectra to vary independently in every annular region, so that the spatial and spectral variation of each component are taken into account. The average temperature in all of the annular regions are found to be the same within statistical uncertainties with  $\log(T_{avg}/K) = 6.1 \pm 0.1$ , indicating an isothermal medium. As the galaxy is not at the center of the field (figure 1, left panel), we cannot extract complete annuli beyond 100kpc ( $r_{\perp}$ ) from the center of the galaxy, and miss a fraction of the CGM emission. We correct for the area of those segments, assuming an isotropic/azimuthally symmetric emission from the CGM of NGC 3221, to obtain the cumulative emission integral profile over the spherical volume around NGC 3221. In figure 7 we show the radial profile of the EI. At smaller radii, it increases with radius, and then flattens. A local source like LHB and/or MWH would have almost uniform surface brightness over the galaxy-field. Hence, their emission integral will be proportional to radius squared, overshooting the saturated profile observed in figure 7. This reinstates that the detected signal is from the CGM of NGC 3221 with a radially falling surface brightness (as also seen in figure 4), and eliminates the possibility of it being a Galactic emission. As the emission integral is a cumulative measurement, its saturation indicates how far the warm-hot diffuse medium is extended. We find that the radial profile of emission integral becomes flat beyond 150 kpc from the center of NGC 3221, giving a rough estimate of the spatial extent of the CGM of the galaxy down to our sensitivity limit.

#### 4.3. Modeling

Our next goal is to estimate the density, spatial extent and the total baryonic mass contained in the CGM of

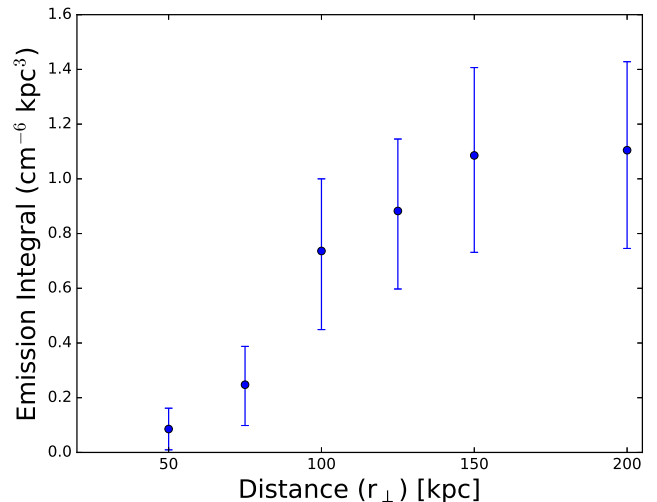


**Figure 7.** The radial profile of the emission integral (EI) of the warm-hot CGM of NGC 3221

NGC 3221, given that the detected signal is truly from NGC 3221. We calculate the average emission measure (EM) profile from the cumulative emission integral profile. As the emission integral of the larger annulus encompasses the emission integral of the smaller annulus, the uncertainties are not independent. We assume that the correlation coefficient of the consecutive measurements is 0.5, i.e. the covariance is half the geometric mean of their own variance:  $\sigma_{i,i-1} = 0.5\sigma_i\sigma_{i-1}$ . We fit the EM profile with a  $\beta$ -model. The  $\beta$ -model (eqn. 3) has a density profile:

$$n = n_o(1 + (r_{\perp}/r_c)^2)^{-\frac{3\beta}{2}} \quad (3)$$

where  $n_o$  is the central density and  $r_c$  is the core radius, resulting in an EM profile similar to the surface brightness profile (eqn. 4) (Sarazin 1986),

$$EM = EM_o(1 + (r_{\perp}/r_c)^2)^{-3\beta+0.5} \quad (4)$$

where  $EM_o$  is the central emission measure. Because of the small number of data points, large error bars and the degeneracy between the parameters, we could not fit the three parameters of the  $\beta$ -model simultaneously. Therefore, as we did for the surface brightness profile in §3.1, we fit the EM profile in two different ways.

1) A  $\beta$ -model: We first fixed  $\beta = 0.5$  and fit the radial profile for  $EM_o$  and  $r_c$ . Then we fix  $r_c$  to the best-fit value (152.4 kpc) and fit for  $EM_o$  and  $\beta$ . The resulting fit ( $\chi^2/dof = 3.3/4$ ) yielded parameters values:  $EM_o = (2.8 \pm 1.1) \times 10^{-5} \text{ cm}^{-6} \text{ kpc}$  and  $\beta = 0.56 \pm 0.36$ . We could not determine the range of  $r_c$  from the fit, but we obtain the range of  $r_c$  empirically for the best-fitted values of  $EM_o$  and  $\beta$  which is consistent with the  $1\sigma$  error span of the emission measure profile, with minimum

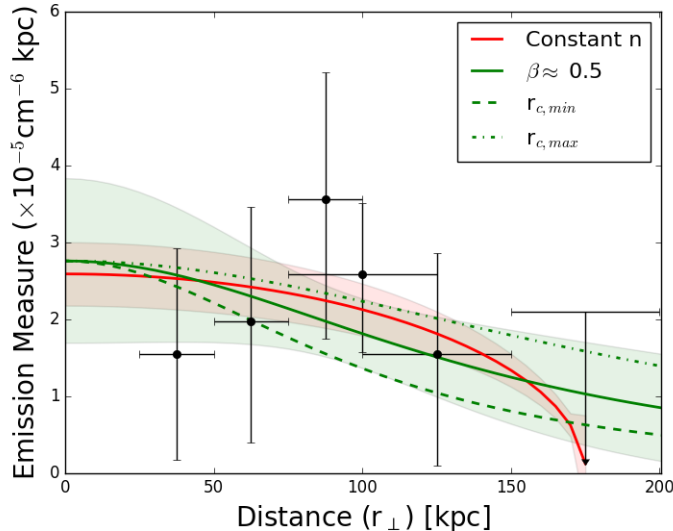


**Figure 8.** Radial profile of emission measure (EM). The best-fitted constant density and  $\beta$ -model with  $\beta \sim 0.5$  are shown, with shaded regions describing  $1\sigma$  ranges. As we do not have any measurement at the center, the uncertainty at  $r=0$  is quite high. The allowed range of  $r_c$  ([110,225] kpc for model A) for the best-fitted values of  $EM_o$  and  $\beta$  has been calculated empirically

$r_c = 110$  kpc and maximum  $r_c = 225$  kpc. Interestingly, the best-fitted values and the confidence intervals are consistent with those obtained by fitting the radial profile of surface brightness in §3.1. Additionally, we fit the EM profile with Model B, a constant density model. 2) A constant density model: The truncated constant density homogeneous medium ( $n = n_o(\text{constant})$ ), has an elliptical profile of projected EM (eqn. 5),

$$EM = 2n_o^2 R_{out} \sqrt{1 - (r_{\perp}/R_{out})^2} \quad (5)$$

where  $R_{out}$  is the spatial extent of the gaseous medium. We obtain best-fitted ( $\chi^2/\text{dof} = 1.4/4$ ) values of  $n = \sqrt{n_i n_e} = (2.7 \pm 0.2) \times 10^{-4} \text{cm}^{-3}$  and  $R_{out} = 175 \pm 2$  kpc (figure 8).

#### 4.4. Physical characterization

We calculate the mass of the gaseous halo and the central electron density assuming  $n_e = 1.3n_i$  and the mean atomic mass  $\mu = 0.62$ , the estimates for fully ionized gas of solar metallicity. The mass in the constant density model (Model B) measured out to  $R_{out} = 175 \text{kpc}$  is  $(17 \pm 1) \times 10^{10} M_{\odot}$  and  $n_e = 3 \times 10^{-4} \text{cm}^{-3}$ . For the  $\beta$ -model (Model A), we calculate the central electron density using eqn 6

$$n_{eo}n_{io} = \frac{EM_o}{2 \int_0^{R_{out}} (1 + (r/r_c)^2)^{-3\beta} dr} \quad (6)$$

**Table 3.** Mass and density estimates (assuming  $Z = Z_{\odot}$ ) of the warm-hot CGM for the  $\beta$  model

$R_{out}[\text{kpc}]$	Mass[ $10^{10} M_{\odot}$ ]	$n_{eo}[10^{-4} \text{cm}^{-3}]$
150	$10.16 \pm 1.69$	$4.16 \pm 0.69$
175	$14.221 \pm 2.248$	$4.03 \pm 0.64$
200	$18.868 \pm 2.903$	$3.94 \pm 0.60$
253	$31.38^{+9.17}_{-7.80}$	$3.80 \pm 0.59$

and the mass using eqn. 7,

$$M = 4\pi(n_{eo} + n_{io})\mu m_H \int_0^{R_{out}} (1 + (r/r_c)^2)^{-\frac{3\beta}{2}} r^2 dr \quad (7)$$

and quote the values in table 3. All these mass values are quoted for solar metallicity. Since the halo metallicity is likely sub-solar (e.g. Gupta et al. 2012; Prochaska et al. 2017), and the estimated halo mass is inversely related to metallicity, these values are lower limits. We confidently detect the CGM emission out to 150 kpc, so the first outer radius is set to  $R_{out} = 150$  kpc. The constant density model has a cutoff radius of 175 kpc, so we calculate mass within 175 kpc as well. The *Suzaku* field of view extends to 200 kpc, so we calculate the mass and density parameters  $R_{out} = 200$  kpc as well, even though the photon count rate within 200 kpc and 150 kpc is small. The region beyond 200 kpc is outside the field of view of *Suzaku*; therefore to calculate the CGM mass within the virial radius of the galaxy (calculated below), we extrapolate the  $\beta$ -profile out to the virial radius  $R_{200} = 253$  kpc (see Table 3).

We compare the mass estimates of the two models out to 150 kpc. In the  $\beta$ -model, the mass is  $(10 \pm 2) \times 10^{10} M_{\odot}$  and in the constant density model it is  $(11 \pm 1) \times 10^{10} M_{\odot}$ . Thus the mass estimates in the two models are consistent with each other, showing that the mass measurement is convergent.

We estimate the virial mass ( $\simeq M_{200}$ ) of NGC 3221 from the maximum rotational velocity of the galaxy ( $V_{max}$ ) using the baryonic Tully-Fisher relation for cold dark matter cosmology. We take the average of 14 measurements of  $V_{max}$  from HyperLeda catalog<sup>2</sup>, which gives  $V_{max} = 269 \pm 18 \text{ km s}^{-1}$ . We calculate  $M_{200}$  using eqn. 8 from the numerical results of Navarro et al. (1997),

$$\log\left(\frac{M_{200}}{10^{10} M_{\odot}}\right) = -5.31 + (3.23 \pm 0.03)\log(V_{max}) \quad (8)$$

<sup>2</sup> <http://leda.univ-lyon1.fr/> (Makarov et al. 2014)

and obtain  $M_{200} = (3.44 \pm 0.94) \times 10^{12} M_{\odot}$ . We compute the virial radius ( $\simeq R_{200}$ ) from  $M_{200}$  using eqn. 9,

$$M_{200} = 200 \times \frac{4\pi}{3} \rho_{crit} R_{200}^3 \quad (9)$$

where  $\rho_{crit}$  is the critical density of the universe. We thus estimate  $R_{200} = 253 \pm 23$  kpc. The virial temperature is:

$$T_{vir} = \frac{GM_{200}m_{eqv}}{3k_B R_{200}}; m_{eqv} = \mu(m_p + m_e) \quad (10)$$

We find that  $T_{vir} = 1.5 \pm 0.4 \times 10^6$  K is comparable with the average temperature of the warm-hot CGM, showing that the CGM can be in thermal and hydrostatic equilibrium.

We further compare the predicted value of  $\beta$  with the value we obtain from the data. For an isothermal hydrostatic gas, Sarazin (1986) predicts that the  $\beta$  index is linked to the ratio of gravitational and thermal energy density in the form of eqn. 11,

$$\beta_{predict} = \mu m_H \sigma_v^2 / 3k_B T_X \quad (11)$$

where  $\sigma_v$  and  $T_X$  are the velocity dispersion of the galaxy and the average temperature of the warm-hot halo gas respectively. Neglecting the difference between  $V_c$  and  $V_{max}$ , we calculate  $\sigma_v$  from Corsini et al. (2004):

$$V_c = (1.32 \pm 0.09) \sigma_v + (46 \pm 14). \quad (12)$$

We use  $T_X = T_{avg}$  and  $\mu=0.62$  as reported and discussed in §4.1 and §4.4 respectively. There are 14 studies available in HyperLeda catalog giving a wide range of values of  $V_{max}$ , from  $V_{max} = 234.9 \pm 0.8$  km/s (Wong et al. 2006) to  $291.05 \pm 8.0$  km/s (Schneider et al. 1990), with a mean of  $268.65 \pm 18.0$  km/s. Using these values, we obtain a range of  $\beta_{predict}$  from  $0.4 \pm 0.1$  to  $0.7 \pm 0.1$ , with a central value of  $\beta_{predict} = 0.6 \pm 0.1$ . This is similar to the best-fit  $\beta = 0.56 \pm 0.36$  obtained for the  $\beta$ -model radial density profile in §4.3. Thus the warm-hot CGM in NGC 3221 appears to be a isothermal hydrostatic system.

## 5. DISCUSSION

Assuming that our detection of the emission from the warm-hot CGM of NGC 3221 is true, we have determined the physical parameters of the CGM such as its temperature, density profile and mass, with a varying degree of uncertainty (§4). Similarly, in the following subsections we use the measured and derived parameters to draw interesting inferences on the missing feedback, missing baryons, and missing metals problems.

### 5.1. Missing feedback

Wang (2010) showed that the X-ray luminosity of hot gas in galaxies is only a few percent of the energy injected by supernovae; this is called the ‘‘missing feedback’’ problem. With our detection of a large amount of warm-hot gas in the CGM of NGC 3221 we investigate the role of starburst-driven winds and supernovae on the physical characteristics of the CGM and their relevance to the missing feedback problem.

#### 5.1.1. The role of starburst-driven winds

The metals in the CGM come from the stellar winds and supernova feedback. Because we have detected Oxygen in the warm-hot CGM of NGC 3221, it is necessary to check if the stellar feedback of the galaxy can actually enrich the CGM with metals. According to the standard superbubble theory of disk galaxies (Mac Low & McCray 1988), the blowout of the gas from the galaxies is determined by the energy injection rate per unit disc area. Following Henley et al. (2010), we calculate the SN rate from  $R_{SN} = 0.2 L_{FIR} / 10^{11} L_{\odot}$  and obtain the specific SN rate  $F_{SN} = R_{SN} / (0.25\pi D_{25}^2)$  (Strickland et al. 2004) to be  $\approx 88 \text{ Myr}^{-1} \text{ kpc}^{-2}$ . This value is much larger than the critical surface rate for superbubble blowout of  $F_{SN} > 25\text{-}40 \text{ Myr}^{-1} \text{ kpc}^{-2}$  (Mac Low & McCray 1988), indicating that the warm-hot X-ray corona can be potentially enriched by the starburst-driven winds, leading to non-zero metallicity of the gaseous medium.

#### 5.1.2. Energy budget of the galactic corona

For the total energy output from supernovae (SNe), we assuming  $10^{51}$  erg per SN. The explosion rate of Type Ia SNe is calculated using Mannucci et al. (2005):

$$\nu_{Ia} = 0.044 (M_{\star} / 10^{10} M_{\odot}) \text{ century}^{-1} \quad (13)$$

and that of core-collapse (CC) SNe is calculated using Heckman et al. (1990):

$$\nu_{CC} = 0.77 (SFR / M_{\odot} \text{ yr}^{-1}) \text{ century}^{-1} \quad (14)$$

Using the value of  $M_{\star}$  and SFR from table 1, we obtain  $\dot{E}_{SN} = \dot{E}_{Ia} + \dot{E}_{CC} = (1.4 \pm 0.2) + (24 \pm 3) \times 10^{41} \text{ erg s}^{-1}$ . The X-ray (0.1-2.0 keV) luminosity  $L_X$  within 150 kpc (the extent out to which significant emission is detected) is  $\approx 5.1_{-1.5}^{+1.7} \times 10^{41} \text{ erg s}^{-1}$ . Thus, the X-ray radiation efficiency is  $\eta = L_X / \dot{E}_{SN} \approx 0.2 \pm 0.1$ . This indicates that a significant fraction ( $\approx 10 - 30\%$ ) of SNe energy has been converted into soft X-ray emission, alleviating the missing feedback problem. The rest of the energy would be in the hot gas beyond 150 kpc, in the hot gas that cooled, and in the mechanical energy of the outflow.

## 5.2. Missing Baryons

In order to determine the baryon census of NGC 3221, we consider the warm-hot CGM mass (modulo metallicity), the mass of other phases of CGM, the mass of stellar and ISM components, and the virial mass.

### 5.2.1. Baryonic mass

We first consider the mass in the warm-hot phase that we detect with *Suzaku*. In table 3 we have presented the mass for solar metallicity. However, the mass depends (inversely) on the metallicity:

$$M(Z) = M \times \left( \frac{Z}{Z_\odot} \right)^{-0.5} \quad (15)$$

The metallicity is a significant unknown in the derived mass of the warm-hot CGM. The differences in the predicted mass due to different density profiles are negligible compared to the differences caused by the (unknown) metallicity. The warm-hot CGM mass for  $\frac{1}{3} Z_\odot$  at a conservative radius of 150 kpc is  $M_{hot,halo} = 15.8 \pm 2.6 \times 10^{10} M_\odot$  (table 4). This shows that the warm-hot CGM of NGC 3221 harbors a huge amount of gas.

In table 4, we have included the cold ( $T < 10^4 K$ ), cool ( $T \approx 10^4 - 5 K$ ) and warm ( $T \approx 10^5 - 6 K$ ) phases of the CGM, obtained from literature for  $L^*$  galaxies. We find that the warm-hot gas is the most dominant mass component accounting for  $53 \pm 9\%$  of the CGM mass.

Next, we compare the warm-hot gas mass to the disk mass ( $M_{disk}$ ). We get  $M(HI)$  and  $M(H_2)$  from Thomas et al. (2002), and calculate the interstellar dust mass using eqn. 16 from Peebles et al. (2014),

$$\log(M_{dust}/M_\odot) = 0.86 \log(M_*/M_\odot) - 1.31 \quad (16)$$

By adding all these components to the stellar mass, we obtain  $M_{disk} = (M_* + M(HI) + M(H_2) + M_{dust}) \simeq 12 \pm 1 \times 10^{10} M_\odot$ . We see that the mass in the warm-hot CGM is more than that in the galactic disk; this is similar to what was found for the Milky Way (Gupta et al. 2012; Nicastro et al. 2016b).

### 5.2.2. Baryon fraction

It is of interest to know whether the baryons in the warm-hot CGM can account for the missing baryons of NGC 3221. We calculate the baryon fraction  $f_b = \frac{M_{b,tot}}{M_{vir}}$  and compare that to the cosmological baryon fraction  $f_{b,cosmo} = 0.157 \pm 0.001$  (Planck Collaboration et al. 2016). We calculate the total baryonic mass of NGC 3221 ( $M_{b,tot}$ ) by adding the mass in the disk ( $M_{disk}$ ) to the mass in the halo ( $M_{b,halo}$ ). However, the calculation of  $f_b$  is complicated by the fact that the virial mass of NGC 3221 is highly uncertain, with different studies providing different values of the rotational

**Table 4.** Mass budget of NGC 3221

Phase	Mass ( $M_\odot$ )
$M_*$	$10.00 \pm 1.26 \times 10^{10}$
$M_{HI}$	$1.64 \pm 0.20 \times 10^{10a}$
$M_{H_2}$	$8.59 \times 10^{8b}$
$M_{dust,ISM}$	$1.41 \pm 0.15 \times 10^8$
$M_{disk}$	$11.74 \pm 1.28 \times 10^{10}$
$M_{dust,halo}$	$5.00 \times 10^{7c}$
$M_{cold,halo}$	$3.80 \pm 0.72 \times 10^{8d}$
$M_{cool,halo}$	$9.20 \pm 4.30 \times 10^{10e}$
$M_{warm,halo}$	$4.53 \pm 0.75 \times 10^{10f}$
$M_{hot,halo}$	$15.77 \pm 2.62 \times 10^{10g}$
$M_{b,halo}$	$29.54 \pm 5.09 \times 10^{10}$
$M_{b,tot}$	$41.28 \pm 5.25 \times 10^{10}$
$M_{vir}$	$3.44 \pm 0.94_{-1.58}^{+1.87} \times 10^{12h}$

<sup>a</sup>Using the value of  $D_L$  from table 1, and combining the statistical uncertainty and the calibration error of  $(0.11 \pm 0.16) \times 10^{10} M_\odot$

<sup>b</sup>Corrected using the updated value of CO-to- $H_2$  conversion factor from Yao et al. (2003)

<sup>c</sup>Obtained from Ménard et al. (2010)

<sup>d</sup>Calculated for  $Z = Z_\odot$  using the median value of  $M_{CaII,halo}$  for high-mass star-forming galaxies from Zhu & Ménard (2013)

<sup>e</sup>Taken from Prochaska et al. (2017) for the gas out to 160 kpc

<sup>f</sup>Calculated using the ratio of warm and hot gas from the fiducial model of Faerman et al. (2017) and the mass of the hot gas we obtain in our work. As the temperature of the CGM of the galaxies in their model is similar to ours, we assume that the relative abundance of the warm and the hot gas remains same

<sup>g</sup>The mass within 150 kpc at  $Z = \frac{1}{3} Z_\odot$ , the median metallicity of cool CGM at low redshift (Prochaska et al. 2017)

<sup>h</sup>Hyperleada catalog (Makarov et al. 2014)

velocity (see §4.4). This leads to a factor of 2 dispersion in the estimated virial mass, and similar systematic uncertainty in the baryon fraction. The baryon fraction of the hot CGM is  $f_{b,hot} = \frac{M_{hot,halo}}{M_{vir}} = 0.080 \pm 0.023_{-0.032}^{+0.068} (Z/\frac{1}{3}Z_\odot)^{-0.5}$ , showing that it is the reservoir of at least 50% baryons of the baryon budget of NGC 3221. The total baryon fraction is  $f_b = 0.120 \pm 0.036_{-0.048}^{+0.104}$ . This clearly closes the baryon budget of NGC 3221.

The uncertainty in the baryon fraction is three-fold. First, the statistical uncertainty of the detected signal is propagated to the density profile and hence, the mass of the warm-hot CGM. Second, the metallicity adds a factor of few systematic uncertainty to the mass of the warm-hot CGM. The uncertainty in the virial mass, however, is the major source of uncertainty in  $f_b$ .

## 5.3. Missing metals

In addition to the missing baryons problem discussed above, there appears to be a missing metals problem (Peebles et al. 2014). The total mass of metals produced in the universe appears to be much larger than

that found in galaxies. In our discovery of the warm-hot gas in the CGM of NGC 3221, what we actually detect is Oxygen, so we are in a good position to determine whether metals in the CGM alleviate the missing metals problem.

The total mass of the metals expected to be produced in a galaxy with the stellar mass of NGC 3221 is  $M_{metal,expect} = 6.31 \pm 0.80 \times 10^9 M_{\odot}$ , and the metals found in stars, ISM and interstellar dust is only  $M_{metal,disk} \approx 1.99 \times 10^9 M_{\odot}$  (Peeples et al. 2014). We calculate the mass of metals in the X-ray emitting warm-hot phase as a function of metallicity from the mass of the warm-hot halo gas within 150 kpc. We assume the bulk mass fraction of metals in the Sun to be  $Z_{frac} = 0.0142$  (Asplund et al. 2009). The metal fraction is then  $f_{metal} = \frac{M_{metal,found}}{M_{metal,expected}}$ , where  $M_{metal,found} = M_{metal,disk} + M_{metal,CGM}$ . The metal fraction within 150 kpc is  $0.45^{+0.13}_{-0.10}$  for  $\frac{1}{3}Z_{\odot}$ ; and it ranges from about 0.30 to 0.71, increasing slowly with metallicity from 0.1 to 1.0  $Z_{\odot}$ . Thus we see that about 30-70% of the metals are still missing within the observed volume of the CGM. This suggests that a large fraction of the galactic metals got expelled at a larger distance, within and beyond the CGM. This is consistent with earlier observations (Peeples et al. 2014) and the results from the 3D, high-resolution hydrodynamic simulations (Li et al. 2017b), showing that metals are preferentially expelled from a galaxy.

## 6. COMPARISON WITH EARLIER OBSERVATIONS

Gupta et al. (2012) combined their column density measurements of  $z=0$  O VII and O VIII absorption lines with the emission measure of MW halo from literature, and found a massive warm-hot ( $T \approx 10^{6.1-6.4}K$ ) CGM extended out to  $239 \pm 100$  kpc. The mass calculated for solar abundance was  $1.2 \times 10^{10} M_{\odot}$ , being comparable with the baryonic mass of the disk  $\approx 6 \times 10^{10} M_{\odot}$ . They showed that the baryonic fraction  $f_b$  of this warm-hot gas varies from 0.09 to 0.23 depending on the estimates of  $M_{vir} = (1.0-2.5) \times 10^{12} M_{\odot}$ , bracketing the universal value of  $f_b$ . This was later confirmed by Nicastro et al. (2016b), using independent observations.

However, the picture is quite different around other MW-type spiral galaxies. Using *Chandra* observations, Strickland et al. (2004) found diffuse X-ray emitting halos around eight nearby ( $D < 17$  Mpc) galaxies extending only out to  $\approx 10$  kpc. With *XMM-Newton*, Tüllmann et al. (2006) searched for the soft X-ray emission around 9 nearby star-forming galaxies, and did not find any diffuse emission beyond 4-10 kpc around the disk, after correcting for projection. Yamasaki et al. (2009)

using *Suzaku* observation detected the X-ray halo of NGC 4631 ( $D \approx 8$  Mpc) extending out to about 10 kpc from the galactic disk. Bogdán et al. (2015) searched for hot gaseous coronae around 8 nearby ( $14 < D < 40$  Mpc) normal ( $SFR < 10 M_{\odot} yr^{-1}$ ) spiral galaxies with  $M_{\star} \approx (0.7 - 2.0) \times 10^{11} M_{\odot}$  using *Chandra* observations (see also Li & Wang 2013). They did not detect any statistically significant diffuse X-ray emission beyond the optical radii ( $\approx 20$  kpc) of the galaxies. Thus all the detections were of extra-planar gas, not of the extended CGM. The non-detections were caused by a variety of reasons: either the observations were too shallow ( $t_{exp} \approx 8-55$  ks), or the choice of the detectors was not optimal (i.e. they had small field-of-view and/or small effective area), or the targets were so close that only a small fraction of the halo was within the field-of-view, or the targets were so far that the emission was too faint to be detected in the observed time. Additionally, in the spectral analyses, the sky backgrounds were often extracted from the same fields of the targets, usually from regions within the virial radii. Thus, if the CGM is extended out to the virial radii, the backgrounds would be overestimated and the CGM signal would be underestimated. Therefore, the non-detections of the CGM in other MW-like external galaxies are likely the effect of observational designs and/or analysis methods, rather than the intrinsic properties of the galaxies themselves.

On the other hand, searches for the CGM emission around individual and stacked massive spirals yielded detections (Anderson & Bregman 2011; Dai et al. 2012; Bogdán et al. 2013b; Anderson et al. 2016; Li et al. 2017a; Bogdán et al. 2017; Li et al. 2018; Bregman et al. 2018). The masses of hot extended gaseous halos were found to be huge, but the virial masses were too large, so the total baryon fraction was small, with  $f_b \leq 0.1$ .

Thus, we can summarize the previous work on X-ray observations of the CGM as follows: (1) in the MW, a large mass of warm-hot gas is detected that can close the baryon census; (2) in other MW-type galaxies, the mass of the hot gas, if detected, is not significant, though this is likely an observational bias; and (3) in massive galaxies, a large mass of hot gas is detected, but it is insufficient to account for the missing baryons. Tüllmann et al. (2006) observed NGC 3221 with *XMM-Newton*. Since they did not detect the CGM of this galaxy while we did with our *Suzaku* observations, it is imperative to understand why. In their imaging analysis, Tüllmann et al. (2006) performed contour mapping of the soft X-ray image of the galaxy, including the disk. The surface brightness of the disk and the foreground (local/Galactic) sources are much higher than that of the halo gas, therefore the contours were not sensitive to the

faint extended emission. In our imaging analysis, we removed the inner 25 kpc region around the galaxy (§2.2; figure 1, left panel), and focused on the region beyond that. This ensured that the X-ray emission we study is not contaminated by the galaxy itself. With our quantitative imaging analysis we find an indirect evidence of the halo gas (§3.1, figure 4). Additionally, we performed a detailed and intricate spectral analysis (§3.2), where the galaxy-field is simultaneously fitted with two blank sky observations to estimate the foreground, background and the atmospheric contamination (figure 6). This was crucial in extracting the weak CGM signal, but there is no spectral analysis in Tüllmann et al. (2006). To conclude, we detected the CGM of NGC 3221, but Tüllmann et al. (2006) did not, because of a combination of differences in imaging and spectral analysis.

Ours is the first discovery of the warm-hot CGM of an L\* galaxy, with a  $3.4\sigma$  significance, extended out to at least 150 kpc from the center of the galaxy. For a metallicity of  $\frac{1}{3}Z_{\odot}$ , the warm-hot gas accounts for  $53\pm 9\%$  of the CGM mass and  $38\pm 5\%$  of the total baryonic mass of the galaxy, being the dominant component of all the baryons. It is the first external spiral galaxy accounting for all its missing galactic baryons.

## 7. CONCLUSION AND FUTURE DIRECTIONS

In this paper we have studied the warm-hot X-ray-emitting CGM of an L\* star-forming spiral galaxy NGC 3221, with deep *Suzaku* observations. We re-discovered the O I contamination in *Suzaku* data using a robust spectral modeling taking into account all foreground and background components. The contaminating O I emission line needs to be included in the spectral modeling, otherwise it can result in false detection and/or overestimation of the O VII signal and wrong characterization of the CGM, as in Kataoka et al. (2013); Miller & Bregman (2016). Our science results are as follows:

1) We have detected the warm-hot CGM around NGC 3221 at  $3.4\sigma$  significance out to at least 150 kpc. The bolometric X-ray luminosity of the gas is  $\approx 5 \times 10^{41}$  erg s<sup>-1</sup>. This is the first detection of an extended CGM around an external L\* spiral galaxy.

2) The main uncertainty in estimating the baryon fraction is the virial mass of the galaxy, but we find that  $f_b$  can be consistent with the cosmic value. This is the first external spiral galaxy with all the baryons accounted for. It shows that the warm-hot phase of the CGM of L\* spirals can account for the missing baryons.

3) A significant fraction ( $\approx 20\%$ ) of the supernova energy has been converted in soft X-ray emission, alleviating the missing feedback problem.

4) Our study of the metal fraction in the CGM indicates that the metals are preferentially expelled from the galaxy.

To search for and characterize the warm-hot CGM further, it is essential to study a broad sample of galaxies with a range of  $M_*$ , SFR and  $M_{vir}$ . At present, *XMM-Newton* is the most suitable mission to detect the faint emission from the warm-hot halo gas because of its large effective area and large FOV. On a longer timescale, upcoming missions (e.g. *XRISM*, *Athena*, *Lynx*) in the next decade and beyond will offer an outstanding opportunity to observe the warm-hot diffuse medium in absorption in unprecedented detail. This will bring us closer to understanding galaxy formation and evolution.

## ACKNOWLEDGEMENTS

We gratefully acknowledge support through the NASA ADAP grants NNX16AF49G to SM and 80NSSC18K0419 to AG. Support for this work was also provided by the National Aeronautics and Space Administration through Chandra Award Number 25-10-20-30300-53001 to AG issued by the Chandra X-ray Observatory Center, which is operated by the Smithsonian Astrophysical Observatory for and on behalf of the National Aeronautics Space Administration under contract NAS8-03060. YK acknowledges support from the grant PAIIPIT IN106518.

*Facilities:* *Suzaku*

*Software:* HeaSoft v6.17 (Drake 2005), AstroPy v1.1.2 (Astropy Collaboration et al. 2013), NumPy v1.11.0 (Dubois et al. 1996), SciPy v0.17.0, Matplotlib v1.5.3 (Hunter 2007)

## REFERENCES

- Anderson, M. E., & Bregman, J. N. 2011, ApJ, 737, 22
- Anderson, M. E., Churazov, E., & Bregman, J. N. 2016, MNRAS, 455, 227
- Asplund, M., Grevesse, N., Sauval, A. J., & Scott, P. 2009, ARA&A, 47, 481
- Astropy Collaboration, Robitaille, T. P., Tollerud, E. J., et al. 2013, A&A, 558, A33
- Bogdán, Á., Bourdin, H., Forman, W. R., et al. 2017, ApJ, 850, 98
- Bogdán, Á., Forman, W. R., Kraft, R. P., & Jones, C. 2013a, ApJ, 772, 98

- Bogdán, Á., Forman, W. R., Vogelsberger, M., et al. 2013b, *ApJ*, 772, 97
- Bogdán, Á., Vogelsberger, M., Kraft, R. P., et al. 2015, *ApJ*, 804, 72
- Bregman, J. N., Anderson, M. E., Miller, M. J., et al. 2018, *ApJ*, 862, 3
- Corsini, E. M., Pizzella, A., Dalla Bontà, E., et al. 2004, *Memorie della Societa Astronomica Italiana Supplementi*, 5, 249
- Dai, X., Anderson, M. E., Bregman, J. N., & Miller, J. M. 2012, *ApJ*, 755, 107
- Drake, S. A. 2005, in *X-Ray and Radio Connections*, ed. L. O. Sjouwerman & K. K. Dyer (Santa Fe, New Mexico: NRAO), 6.01
- Dubois, P. F., Hinsen, K., & Hugunin, J. 1996, *Computers in Physics*, 10, 262
- Faerman, Y., Sternberg, A., & McKee, C. F. 2017, *ApJ*, 835, 52
- Ford, A. B., Davé, R., Oppenheimer, B. D., et al. 2014, *MNRAS*, 444, 1260
- Forman, W., Jones, C., & Tucker, W. 1985, *ApJ*, 293, 102
- Gupta, A., Mathur, S., Galeazzi, M., & Krongold, Y. 2014, *Ap&SS*, 352, 775
- Gupta, A., Mathur, S., & Krongold, Y. 2017, *ApJ*, 836, 243
- Gupta, A., Mathur, S., Krongold, Y., Nicastro, F., & Galeazzi, M. 2012, *ApJL*, 756, L8
- Heckman, T. M., Armus, L., & Miley, G. K. 1990, *ApJS*, 74, 833
- Henley, D. B., & Shelton, R. L. 2013, *ApJ*, 773, 92
- . 2015, *ApJ*, 808, 22
- Henley, D. B., Shelton, R. L., Cumbee, R. S., & Stancil, P. C. 2015, *ApJ*, 799, 117
- Henley, D. B., Shelton, R. L., Kwak, K., Joung, M. R., & Mac Low, M.-M. 2010, *ApJ*, 723, 935
- Humphrey, P. J., Buote, D. A., O’Sullivan, E., & Ponman, T. J. 2012, *ApJ*, 755, 166
- Hunter, J. D. 2007, *Computing in Science and Engineering*, 9, 90
- Kataoka, J., Tahara, M., Totani, T., et al. 2013, *ApJ*, 779, 57
- Koyamada, S., Misawa, T., Inada, N., et al. 2017, *ApJ*, 851, 88
- Kuntz, K. D., & Snowden, S. L. 2000, *ApJ*, 543, 195
- Lehmer, B. D., Alexander, D. M., Bauer, F. E., et al. 2010, *ApJ*, 724, 559
- Li, J.-T., Bregman, J. N., Wang, Q. D., Crain, R. A., & Anderson, M. E. 2018, *ApJ*, 855, L24
- Li, J.-T., Bregman, J. N., Wang, Q. D., et al. 2017a, *ApJS*, 233, 20
- Li, J.-T., & Wang, Q. D. 2013, *MNRAS*, 428, 2085
- Li, M., Bryan, G. L., & Ostriker, J. P. 2017b, *ApJ*, 841, 101
- Liu, W., Chiao, M., Collier, M. R., et al. 2017, *ApJ*, 834, 33
- Mac Low, M.-M., & McCray, R. 1988, *ApJ*, 324, 776
- Makarov, D., Prugniel, P., Terekhova, N., Courtois, H., & Vaughn, I. 2014, *A&A*, 570, A13
- Mannucci, F., Della Valle, M., Panagia, N., et al. 2005, *A&A*, 433, 807
- Ménard, B., Scranton, R., Fukugita, M., & Richards, G. 2010, *MNRAS*, 405, 1025
- Miller, M. J., & Bregman, J. N. 2015, *ApJ*, 800, 14
- . 2016, *ApJ*, 829, 9
- Navarro, J. F., Frenk, C. S., & White, S. D. M. 1997, *ApJ*, 490, 493
- Nicastro, F., Senatore, F., Gupta, A., et al. 2016a, *MNRAS*, 457, 676
- Nicastro, F., Senatore, F., Krongold, Y., Mathur, S., & Elvis, M. 2016b, *ApJ*, 828, L12
- Oppenheimer, B. D., Crain, R. A., Schaye, J., et al. 2016, *MNRAS*, 460, 2157
- Peeples, M. S., Werk, J. K., Tumlinson, J., et al. 2014, *ApJ*, 786, 54
- Planck Collaboration, Ade, P. A. R., Aghanim, N., et al. 2016, *A&A*, 594, A13
- Prochaska, J. X., Werk, J. K., Worseck, G., et al. 2017, *ApJ*, 837, 169
- Rossa, J., & Dettmar, R. J. 2003, *A&A*, 406, 505
- Sarazin, C. L. 1986, *Reviews of Modern Physics*, 58, 1
- Schneider, S. E., Thuan, T. X., Magri, C., & Wadiak, J. E. 1990, *ApJS*, 72, 245
- Sekiya, N., Yamasaki, N. Y., Mitsuda, K., & Takei, Y. 2014, *PASJ*, 66, L3
- Shapley, A. E., Steidel, C. C., Pettini, M., & Adelberger, K. L. 2003, *ApJ*, 588, 65
- Snowden, S. L., Freyberg, M. J., Kuntz, K. D., & Sanders, W. T. 2000, *ApJS*, 128, 171
- Snowden, S. L., Chiao, M., Collier, M. R., et al. 2014, *ApJ*, 791, L14
- Strickland, D. K., Heckman, T. M., Colbert, E. J. M., Hoopes, C. G., & Weaver, K. A. 2004, *ApJS*, 151, 193
- Suresh, J., Rubin, K. H. R., Kannan, R., et al. 2017, *MNRAS*, 465, 2966
- Thomas, H. C., Dunne, L., Clemens, M. S., et al. 2002, *MNRAS*, 329, 747
- Tüllmann, R., Pietsch, W., Rossa, J., Breitschwerdt, D., & Dettmar, R. J. 2006, *A&A*, 448, 43
- Tumlinson, J., Peeples, M. S., & Werk, J. K. 2017, *ARA&A*, 55, 389
- Wang, Q. D. 2010, *Proceedings of the National Academy of Science*, 107, 7168

- White, S. D. M., Navarro, J. F., Evrard, A. E., & Frenk, C. S. 1993, *Nature*, 366, 429
- White, S. D. M., & Rees, M. J. 1978, *MNRAS*, 183, 341
- Wong, O. I., Ryan-Weber, E. V., Garcia-Appadoo, D. A., et al. 2006, *MNRAS*, 371, 1855
- Yamasaki, N. Y., Sato, K., Mitsuishi, I., & Ohashi, T. 2009, *PASJ*, 61, S291
- Yao, L., Seaquist, E. R., Kuno, N., & Dunne, L. 2003, *ApJ*, 588, 771
- Yoshino, T., Mitsuda, K., Yamasaki, N. Y., et al. 2009, *PASJ*, 61, 805
- Zhu, G., & Ménard, B. 2013, *ApJ*, 773, 16

## APPENDIX

A. DATA REDUCTION OF *SUZAKU*

We have worked with unfiltered event files and reprocessed everything using the updated calibration database. As we do not follow the default conditions of Aepipeline<sup>3</sup> in every step, the data reduction procedure is sketched in brief :

1. Using `ftmerge` we combine the components of 3x3 and 5x5 mode observations separately.
2. We update the time and coordinate information using `xistime` and `xiscoord` respectively. We correct the Euler angles in the attitude file using `aeattcor`, which calculates the effects of the “thermal wobbling” caused by thermal distortions of the satellite bodies. To have an accurate mapping of channel to energy, we update the one-to-one relation between channel no. and energy using `xispi`. We also update the information of pixel quality using `xisputpixelquality` with the latest bad column file. We create the good time intervals (GTI) for each of the 3x3 and 5x5 mode observations using `xisgtigen`.
3. In `xselect` we apply GTI correction; remove hot and flickering pixels using `sisclean` and screen some events based on their grades. We remove the noisy pixels at higher bit, the pixels illuminated by the <sup>55</sup>Fe calibration sources, and the events in the second trailing rows of artificial charge injection at 6keV based on their status information. The effective exposure time after GTI correction reduces to 41 ks for galaxy-field, 30 ks for off-field1, and 23 ks for off-field2.

We remove the events recorded during or within 436 seconds after the passage through South Atlantic Anomaly (SAA). We allow an elevation angle (ELV) of  $> 10$  deg and the elevation angle from the day Earth rim (DYE\_ELV) of  $> 20$  deg to reduce the contamination from Earth’s atmosphere.<sup>4</sup> Also, we impose a strict condition on geomagnetic cut-off rigidity  $COR2 > 8$  to obtain a good enough signal-to-noise ratio by reducing the particle background. It must be clarified that the older version of  $COR2$ ,  $COR$  cannot do the filtering as efficiently as  $COR2$  and hence, the filtered data can be substantially different in the energy range of interest if the updated version is not used.

We find that the proton flux in the solar wind<sup>5</sup> never exceeds the typical threshold of  $2.0 - 4.0 \times 10^8 \text{ cm}^{-2}\text{s}^{-1}$  during the GTI (figure 9), making sure that effect of the geocoronal SWCX (solar wind charge exchange) induced emission is small and stable.

4. We merge the screened 3x3 and 5x5 mode data in `xselect` to obtain the full exposure.

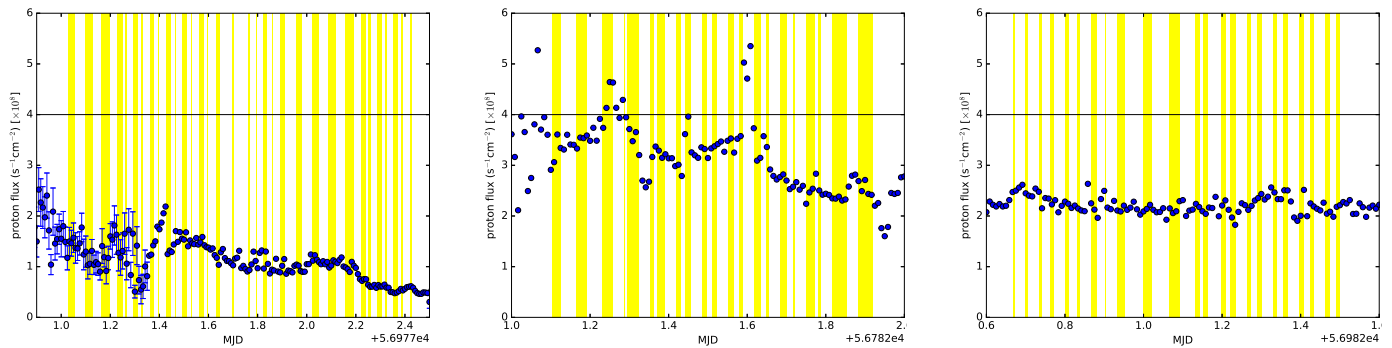


**Figure 9.** Solar wind proton flux during observations. In the middle and right panel the error bars are smaller than the size of data points. The shaded regions are GTIs of respective observations. Left: galaxy-field, middle and right: off-fields

<sup>3</sup> <https://heasarc.gsfc.nasa.gov/docs/suzaku/analysis/abc/>

<sup>4</sup> While a larger cut-off value of DYE\_ELV (e.g.  $> 40$  deg or  $> 60$  deg) removes practically all atmospheric contamination as shown by Sekiya et al. (2014), the signal-to-noise ratio becomes too low to fit a multi-component spectrum. Therefore, we continue with DYE\_ELV  $> 20$  deg, and model the atmospheric contribution as a spectral component.

<sup>5</sup> Data is taken from <http://www.srl.caltech.edu/ACE/ASC/>

Then, we remove the point sources from all fields and remove the galaxy’s contribution from the galaxy-field before extracting the spectra (§2.2).

Using `xisnxbgen` we extract the non X-ray background spectrum (NXB) of each annular region with the latest NXB event file and bad column file. We screen out the events in the second trailing rows of artificial charge injection at 6keV based on its pixel quality.

We extract the redistribution matrix function (RMF) of the whole region using `xisrmfgen`. As the current `xisrmfgen` does not consider spatial variation of spectral response on the CCD chip, which is negligible for the current data, we do not calculate RMF for each annular region separately.

We generate the ancillary response files (ARF) of each annular region using `xissimarfgen` assuming a uniform source of 20’ radius. We include the updated bad column file and remove the second trailing rows of artificial charge injection at 6keV based on its pixel quality.

## B. MODELING THE EMISSION MEASURE PROFILE WITH FREE $\beta$

In the  $\beta$ -model mentioned in the main text, we forced  $\beta$  to be around 0.5, as is assumed for galaxy clusters and the halos of massive galaxies. We can perform a more rigorous analysis by allowing  $\beta$  to be free. We fit for  $EM_o$  and  $r_c$  by varying  $\beta$  in the range of 0.1-1.0 in steps of 0.01, and find that the best fit ( $\chi^2/dof \approx 3.945/4$ ) is obtained for  $\beta = 0.19$ , with the best-fitted  $r_c = 22.19$  kpc. Then, we fit for  $EM_o$  and  $\beta$  keeping  $r_c$  fixed at 22.19 kpc and obtain (with  $\chi^2/dof = 3.662/4$ )  $EM_o = (3.2 \pm 2.6) \times 10^{-5} \text{ cm}^{-6} \text{ kpc}$  and  $\beta = 0.24 \pm 0.10$ . We determine the range of  $r_c$  empirically for the best-fitted values of  $EM_o$  and  $\beta$  which is consistent with the  $1\sigma$  error span of the emission measure profile, with minimum  $r_c = 10$  kpc and maximum  $r_c = 45$  kpc. Interestingly, the best-fitted values and the confidence intervals are consistent with those obtained by fitting the radial profile of surface brightness in §3.1 for both Model A and the free- $\beta$  model. As expected, a steeper  $\beta$  requires a larger core radius  $r_c$  (Model A) and a flatter  $\beta$  has a smaller  $r_c$  (free- $\beta$  model). We find that the mass and the central density of the CGM in the two models (tables 3 and 5) are consistent within  $1\sigma$ . So, with the current data we cannot prefer one model over the other, although  $\chi^2_\nu$  for the model with variable  $\beta$  is closer to 1 than that for the model with constrained  $\beta$ .

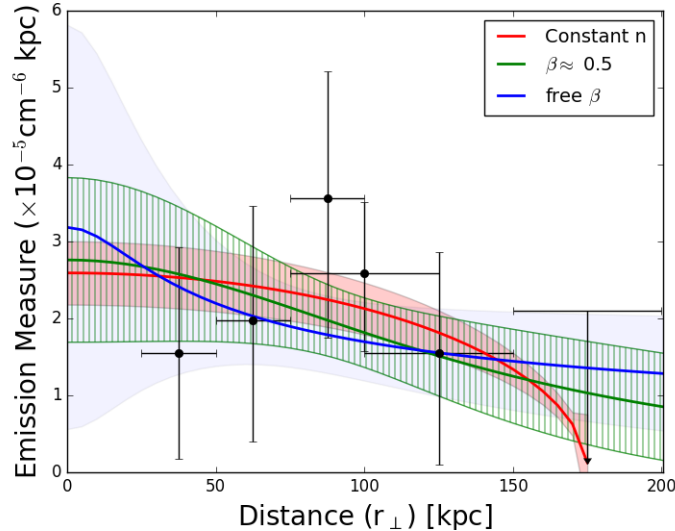


**Figure 10.** Radial profile of emission measure (EM). The best-fitted constant density and  $\beta$ -models with  $\beta \sim 0.5$  and free  $\beta$  are shown, with shaded and hatched regions describing  $1\sigma$  ranges. As we do not have any measurement at the center, the uncertainty at  $r=0$  is quite high.

**Table 5.** Mass and density estimates (assuming  $Z = Z_{\odot}$ ) of the warm-hot CGM for the free- $\beta$  model.

$R_{out}$ [kpc]	Mass[ $10^{10} M_{\odot}$ ]	$n_{eo}$ [ $10^{-4} \text{cm}^{-3}$ ]
150	$7.977 \pm 2.571$	$6.90 \pm 2.22$
175	$11.242 \pm 3.465$	$6.78 \pm 2.09$
200	$15.135 \pm 4.486$	$6.58 \pm 1.85$
253	$26.465^{+12.015}_{-9.971}$	$6.54^{+1.88}_{-1.80}$

### C. ASSUMPTIONS, CAVEATS AND UNCERTAINTIES

We calculate the propagation of uncertainties using the truncated series expansion of error:

$$\sigma_y^2 = \left(\frac{\partial f}{\partial a}\right)^2 \sigma_a^2 + \left(\frac{\partial f}{\partial b}\right)^2 \sigma_b^2 + 2 \left|\frac{\partial f}{\partial a}\right| \left|\frac{\partial f}{\partial b}\right| \sigma_{ab} \quad (\text{C1})$$

where  $y = f(a, b)$ . The variance of (and the covariance between) the fitting parameters of the emission measure profile (central emission measure  $EM_o$ , core radius  $r_c$  and the slope  $\beta$ ) have been used to calculate the uncertainties of (most of) the quantities in §4.4 and §5. As the parameters are strongly correlated (e.g. steeper profile has larger core radius), the uncertainties of the functions are not necessarily of the same order of the uncertainties of the parameters. We should also clarify that the emission measure has been calculated from the cumulative emission integral (EI) as opposed to the differential (bin-by-bin) emission integral. So, the derived errors of the emission measure (figure 8) are subject to the assumption of a moderate covariance between the adjacent annuli. As the surface brightness falls off radially from the galaxy (figure 4), the photon count in the annuli (those we used in §3.1) are not sufficient to extract the CGM's contribution from the multi-component spectrum dominated by the foreground/background. This led us to redesign the annuli size (as discussed in §4.3) and calculate the cumulative EI (figure 7).

We have calculated the mass of the warm-hot halo for the best-fitted value of  $r_c$  assuming full ionization, and with volume-filling factor ( $f_v$ ) and covering factor ( $f_c$ ) of 1. We do not include the errors in  $r_c$  to calculate the uncertainties in the central density, total mass and  $f_b$ . As  $r_c$  is poorly constrained, inclusion of its error reduces the confidence in determining the baryon fraction  $f_b$ , giving us no extra information. The dependence of mass on  $f_{ion} = \frac{n_e}{n_i}$  at a given ionization state is very weak,  $\frac{(f_{ion}+1)}{\sqrt{f_{ion}}}$  decreasing/increasing by a factor of  $\approx 1.01$  from  $Z=Z_{\odot}$  to  $Z=0/5Z_{\odot}$ , respectively. The value of mean atomic mass at a given metallicity is smallest at full ionization, so our calculated value puts the lower limit of the mass of the warm-hot gas. The uncertainty due to absolute metallicity (Metal/H) discussed in §5.2 is based upon the assumption that O/H is a proxy for Metal/H, such that the abundance ratio of Oxygen and other metals are same as solar. Because our data are not sensitive to different chemical compositions, we opt for the solar value, which is the simplest. Also, we have assumed that the ions and the electrons follow the same  $\beta$ -profile. As we find the warm-hot CGM to be isothermal out to 150 kpc, and there is no information about the metallicity gradient, taking  $\frac{n_e}{n_i} =$  radially constant remains a valid assumption. We obtain the number density from the projected emission measure, where any directional property is averaged out. Also, while calculating the emission measure from the emission integral, we assumed that the CGM is isotropic, because we found that any angular dependence of the azimuthal profile of surface brightness out to 100kpc does not affect the radial profile (figure 3).

The absorption study of the internal structure of the CGM (Koyamada et al. 2017) suggests that the high ionization states (e.g. O VI ion) are found in larger clouds and in the diffuse medium than the low ionization states (e.g. C III ion). Extrapolating this for O VII, we assume that the volume-filling factor and covering factor are unlikely to be considerably smaller than 1. Without any measurement of the anisotropy and clumping we cannot estimate  $f_c$ , and thus calculate the mass for  $f_c = 1$  and  $f_v = 1$  only. This is consistent with the semi-analytic models of Faerman et al. (2017) as well.

Our used values of  $M_{\star}$  and  $D_L$  are larger by 4% and  $\approx 8\%$  than some other studies in literature, respectively. However, using the smaller values of these quantities we found that the revised value of  $f_b$  with  $1\sigma$  error bar still brackets the universal value of  $f_b$ .